Journal of Non-Newtonian Fluid Mechanics 240 (2017) 1–14

Contents lists available at ScienceDirect

Journal of Non-Newtonian Fluid Mechanics

journal homepage: www.elsevier.com/locate/jnnfm

Dynamics of spreading thixotropic droplets☆

A.S. Uppal[a,*], R.V. Craster[b], O.K. Matar[a]

[a] Department of Chemical Engineering, Imperial College, London
[b] Department of Mathematics, Imperial College, London

ARTICLE INFO

Article history:
Received 17 October 2016
Revised 4 January 2017
Accepted 7 January 2017
Available online 9 January 2017

Keywords:
Thixotropy
Lubrication theory
Droplets
Spreading

ABSTRACT

The effect of thixotropy on the two-dimensional spreading of a sessile drop is modelled using lubrication theory. Thixotropy is incorporated by the inclusion of a structure parameter, λ, measuring structure build-up governed by an evolution equation linked to the droplet micromechanics. A number of models are derived for λ coupled to the interface dynamics; these range from models that account for the cross-stream dependence of λ to simpler ones in which this dependence is prescribed through appropriate closures. Numerical solution of the governing equations show that thixotropy has a profound effect on the spreading characteristics; the long-time spreading dynamics, however, are shown to be independent of the initial structural state of the droplet. We also compare the predictions of the various models and determine the range of system parameters over which the simple models provide sufficiently good approximations of the full, two-dimensional spreading dynamics.

1. Introduction

Thixotropy is of central importance in a variety of applications, due to its presence in a wide range of fluids, which include natural muds, slurries, clay suspensions, greases, paints, gels and adhesives [1]. The mechanism underlying thixotropy is normally attributed to the interactions of polymers, particles and colloids, for instance, within the fluid capable of forming a microstructure [2]; the evolving microstructure modifies the internal stress of the fluid and consequently alters the rheological response. While in this paper, we will model thixotropy by the direct inclusion of a structure parameter, it has been shown that thixotropy and yield stress behaviour can be the natural limit of viscoelastic behaviour, when the relaxation time is large, [3–5]. Structure parameter models can be seen to be a natural extension of viscoelastic thixotropy models when you take the structure parameter to be the trace of the conformation tensor. Thixotropy can have a dramatic effect upon the flow behaviour as exemplified by the chaotic regimes observed in numerical studies of a highly thixotropic fluid displaced by a Newtonian fluid [6]. Similarly, fingering instabilities are seen to grow exponentially, rather than algebraically during the injection of a thixotropic fluid into a porous medium [7]. Additional flow regimes have also been found when gravity-driven flows of thixotropic fluids have been studied [8–10] Finally, in capillary-driven levelling of a thixotropic fluid [11], large variations in viscosity across a fluid layer were measured. In the present work, we will restrict our analysis to capillary-driven flows where inertia is negligible.

The aforementioned studies have all used the lubrication approximation as a key simplification which exploits the naturally occurring small aspect ratio; this permits solution for the depth dependence of the velocity field, and the derivation of an evolution equation for the interface [12]. It is not possible, however, to remove the depth dependence completely in the presence of thixotropy using lubrication theory. Typically, one is left with a so-called "1.5D model" [13] characterised by a one-dimensional (1D) equation for the interface coupled to a two-dimensional equation for the structure parameter, that must be integrated over the depth. Additional simplifications have been proposed to reduce this further through an averaged structure [10] or 'fluidity' [7]. This is further built upon by Livescu et al. [14] where a depth profile is assumed for the fluidity that is then linked to the structure parameter at the substrate and the interface, yielding three 1D evolution equations. Alternatively, one can assume a depth profile for the structure parameter in the form of a polynomial [15]. Furthermore, an asymptotic approach is considered by Pritchard et al. [16] where the thixotropic properties are considered weak and enter at higher order. Our goal here is to solve a typical problem of interest, the evolution of a spreading droplet, and then assess which, if any, of the above simplifying approximations are appropriate via com-

☆ This document is a collaborative effort.

* Corresponding author.
E-mail address: a.uppal14@imperial.ac.uk (A.S. Uppal).

http://dx.doi.org/10.1016/j.jnnfm.2017.01.001

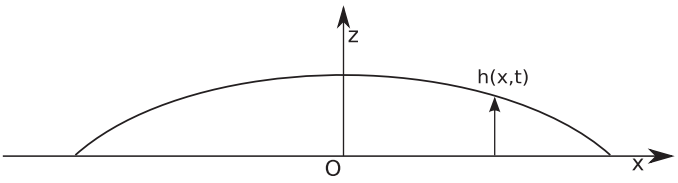

Fig. 1. Schematic illustration of the coordinate system used to model the spreading.

parisons with the solution of the 1.5D model through a parametric study. It is noted by Pritchard et al. [16] that reduced models can be insufficient for confined thixotropic flows, due to the presence of strong transverse gradients in the microstructure. However, this may not hold true for unconfined flows with free surfaces. In this present work, we seek to verify the validity of reduced models with respect to free-surface flows in the presence of moving contact lines.

The rest of this paper is organised as follows. In Section 2, we provide details of the problem formulation, in which we set out the rheological model under consideration via a microstructure derivation of the model. We also derive the governing 1.5D model using the lubrication approximation, and demonstrate its connection to simpler models. In Section 3, we discuss our numerical results, focusing on the comparison of the predictions provided by the various models derived in Section 2. Finally, concluding remarks are provided in Section 4.

2. Formulation

2.1. Governing equations

We consider a slender droplet of density ρ and viscosity $\hat{\mu}$ lying on a horizontal, rigid and impermeable substrate; the overlying gas phase is assumed to be hydrodynamically passive and its dynamics are neglected. We use a Cartesian coordinate system $(\hat{x}, \hat{z})$ with $\hat{x}$ and $\hat{z}$ orientated parallel and normal to the substrate, respectively and with origin at the centreline of the droplet, such that the interface is given by $\hat{z} = \hat{h}(\hat{x}, \hat{t})$, as shown in Fig. 1. The velocity is given by $\hat{\mathbf{u}} = (\hat{u}, \hat{w})$, where $\hat{u}$ and $\hat{w}$ are the components in the $\hat{x}, \hat{z}$ directions, respectively; the hat decoration designates dimensional quantities.

We neglect inertial and gravitational forces such that the governing equations are given by

$$\hat{u}_{\hat{x}} + \hat{w}_{\hat{z}} = 0, \tag{1}$$

$$\hat{\nabla}\hat{p} = \hat{\nabla} \cdot \hat{\tau}, \tag{2}$$

where the stress tensor is expressed by $\hat{\tau}_{ij} = \hat{\mu}(\lambda)\dot{\hat{\gamma}}_{ij}$, $\hat{p}$ denotes the pressure, the rate of strain tensor is given by $\dot{\hat{\gamma}}_{ij} = \partial_j \hat{u}_i + \partial_i \hat{u}_j$, and $|\dot{\hat{\gamma}}| = \sqrt{\dot{\hat{\gamma}}_{ij}\dot{\hat{\gamma}}_{ij}}$ is the second invariant of $\dot{\hat{\gamma}}_{ij}$. Crucially, we assume that the viscosity depends on a dimensionless structure parameter λ that describes the evolving structure within the fluid. We enforce no-slip and no-penetration conditions at the substrate, $\hat{u} = \hat{w} = 0$ at $\hat{z} = 0$ and the kinematic and stress boundary condi-

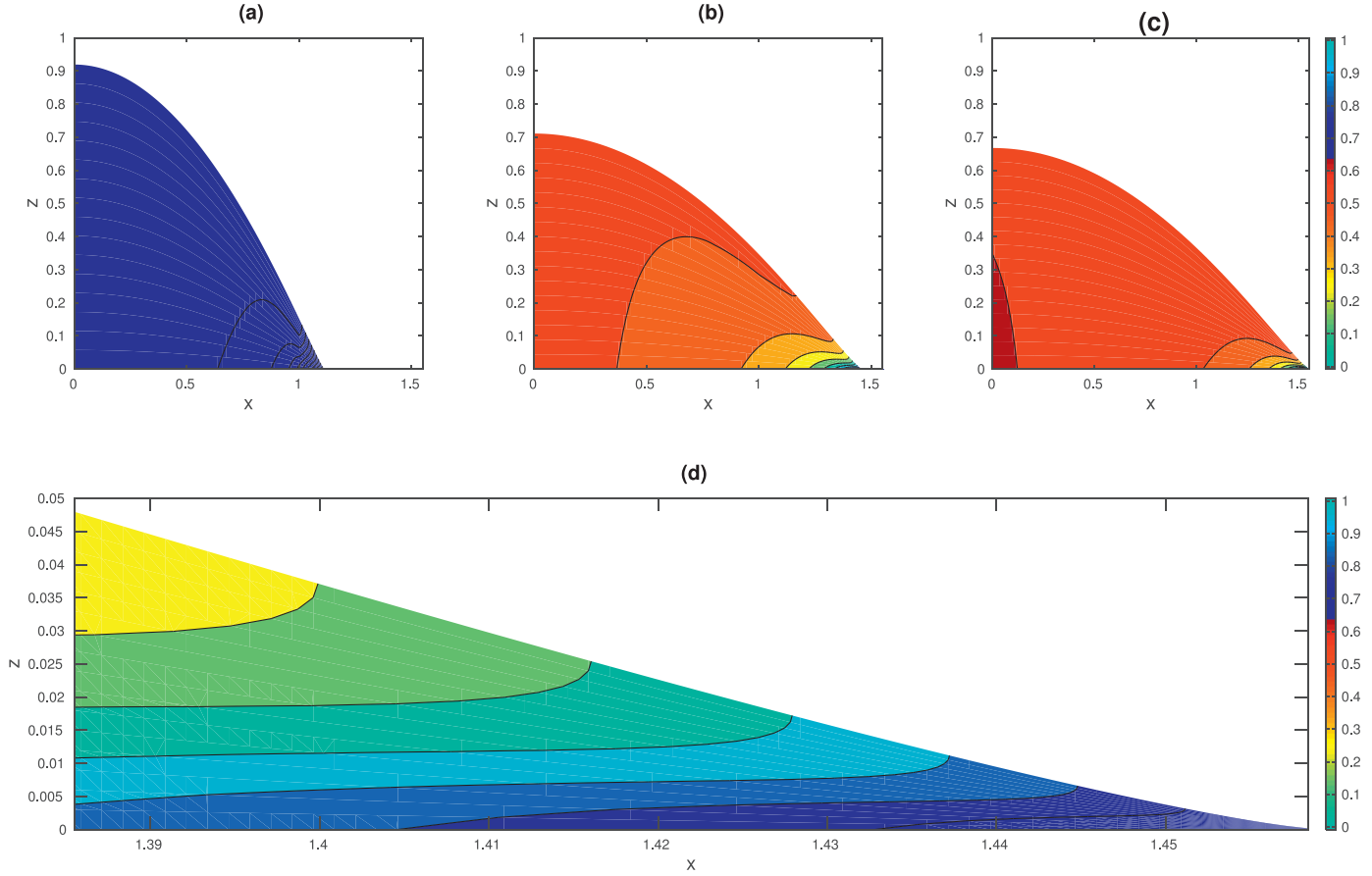

Fig. 2. Results from the numerical solution of Eqs. (20) and (21), computed with $\Lambda = 0$, $B = 5$, $D_b = 10$, and $\delta = 9$: droplet evolution for $t = 1, 25, 50$ shown in (a)-(c), respectively. Panel (d) shows a zoomed in view of the contact line at $t = 25$. In this and subsequent figures, the colour reflects the degree of structure build-up, where red and blue represent high and low values of λ, respectively. (For interpretation of the references to colour in this figure legend, the reader is referred to the web version of this article.)

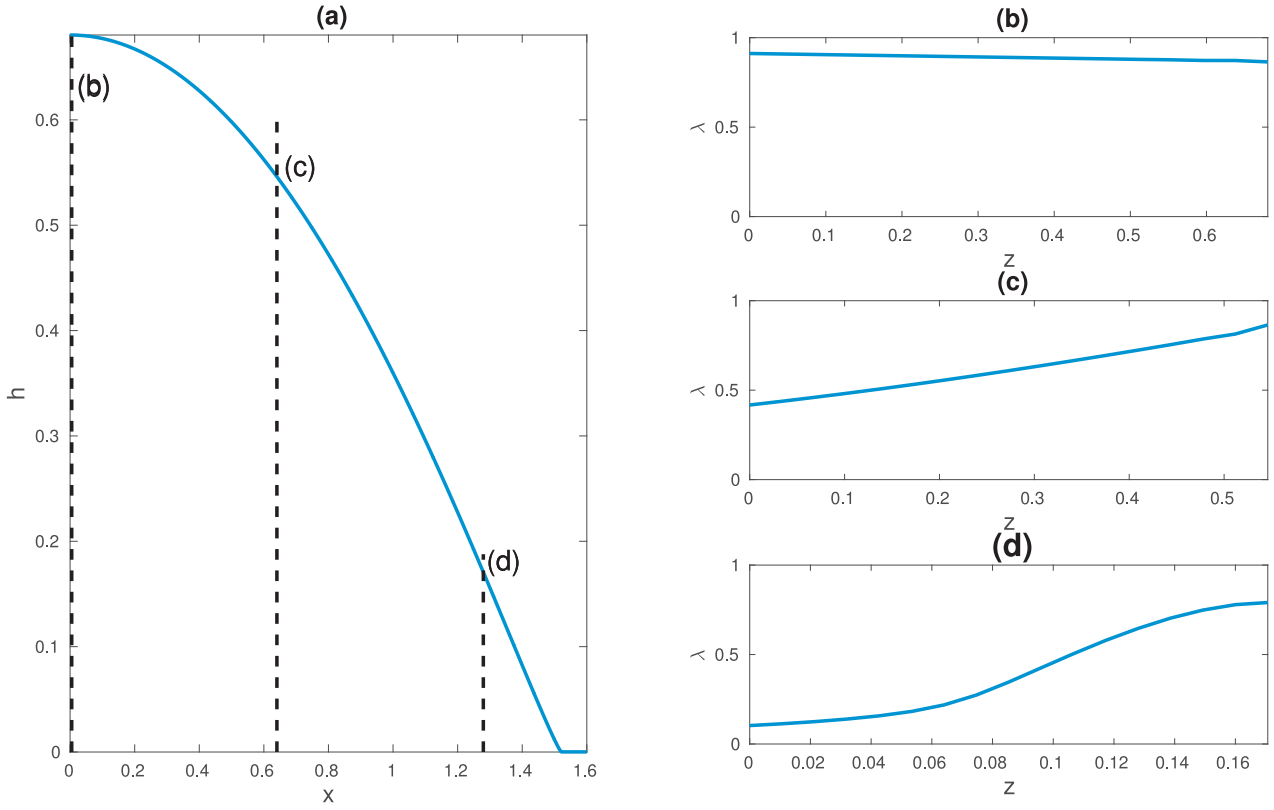

Fig. 3. The dependence of λ in z at various values of x, as shown in (a) for $t = 20$ and for the same values as those used to generate Fig. (2). $\lambda(z)$ is shown at $x = 0$, 0.64 and 1.28, in panels (b)–(d), respectively.

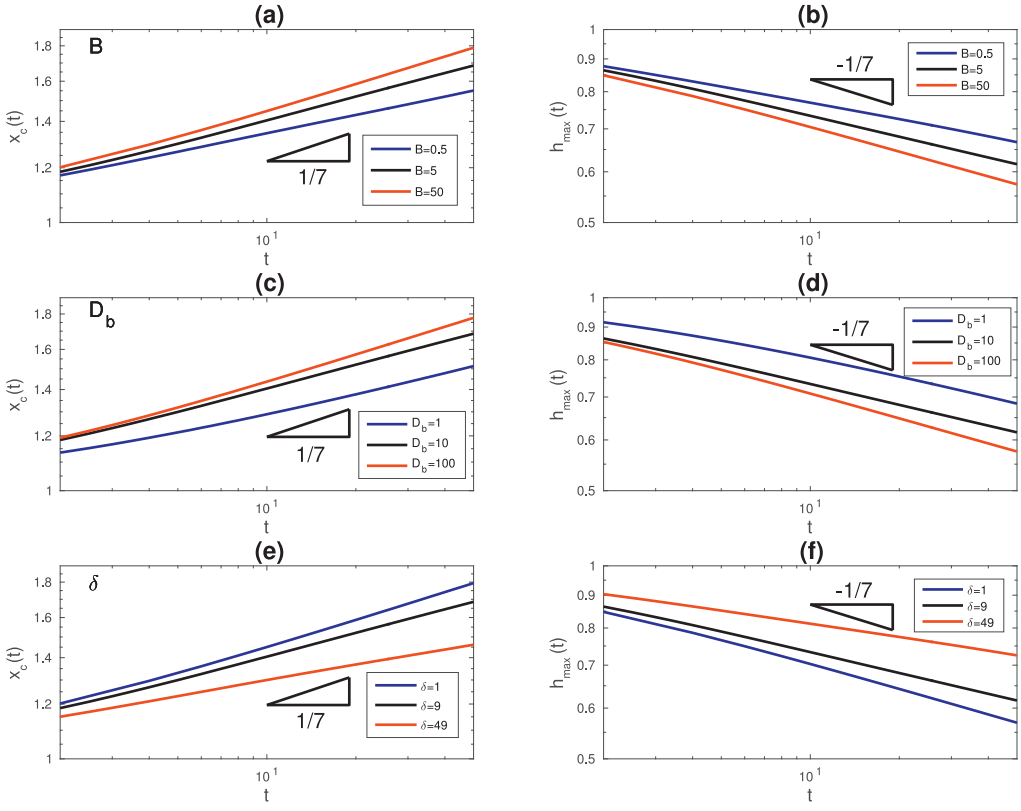

Fig. 4. LogLog plot for the position of the leading edge, $x_c(t)$, (a), (c) (e) and maximum height, h_{max} (b), (d), (f) for different B, D_b and δ values, respectively. Unless stated otherwise, $\Lambda = 0$, $B = 5$, $D_b = 10$ and $\delta = 9$. The slopes of 1.7 and $-1/7$ shown in the panels represent the scaling exponents for x_c and h_{max}, respectively, associated with capillary-driven spreading of a Newtonian fluid drop. (For interpretation of the references to colour in this figure legend, the reader is referred to the web version of this article.)

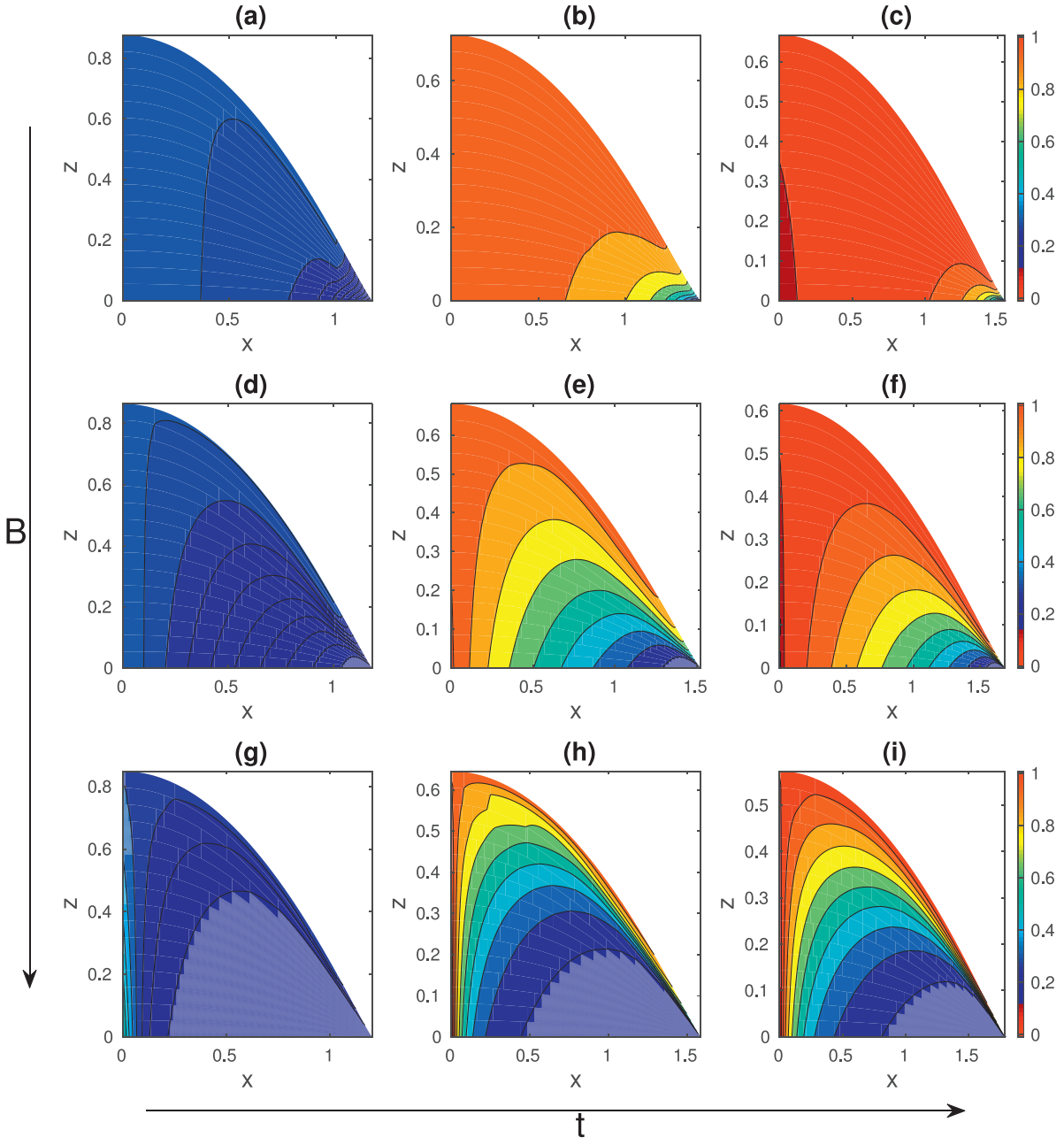

Fig. 5. Snapshots of the λ field at $t = 2$ (a, d, g), 20 (b, e, h) and 50 (c, f, i). We fix $D_b = 10$ and $\delta = 9$ and vary B, where $B = 0.5$ (a, b, c), $B = 5$ (d, e, f) and $B = 50$ (g, h, i). (For interpretation of the references to colour in this figure legend, the reader is referred to the web version of this article.)

tions at $\hat{z} = \hat{h}$, respectively given by,

$$\hat{h}_{\hat{t}} + \hat{u}\hat{h}_{\hat{x}} - \hat{w} = 0, \tag{3}$$

$$\mathbf{n} \cdot \hat{\mathbf{T}} \cdot \mathbf{n} = -\sigma \nabla_s \cdot \mathbf{n}, \tag{4}$$

$$\mathbf{n} \cdot \hat{\mathbf{T}} \cdot \mathbf{t} = 0, \tag{5}$$

where σ denotes the constant surface tension, $\hat{\mathbf{T}} = -p\mathbf{I} + \tau$ in which $\mathbf{I}$ is the identity tensor; $\mathbf{n} = (-\hat{h}_x, 1)/(1 + \hat{h}_x^2)^{1/2}$ and $\mathbf{t} = (1, \hat{h}_x)/(1 + \hat{h}_x^2)^{1/2}$ denote the normal and tangent vectors to the interface, respectively; $\nabla_s = (\mathbf{I} - \mathbf{nn}) \cdot \nabla$ is the surface gradient operator.

2.2. Rheological model

The evolution of the structure parameter, λ, is determined via an approach whereby we assume that the particles within the fluid create, or destroy, linkages or bonds between each other; we take λ to be the ratio of unbroken bonds to the total possible bonds at each point in space [17]. Following this definition, we derive an evolution equation using the approach set out in [18]: we let $n(\mathbf{x}, t)$ denote the number of inter-particle bonds at each point in space and time and $m(\mathbf{x}, t) = n_{max} - n(\mathbf{x}, t)$ the number of broken bonds, where n_{max} is the total possible number of bonds at each point. We assume the formation and breakage of inter-particle bonds to be a reversible stochastic process represented by

$$n \underset{k_f}{\overset{k_b}{\rightleftharpoons}} m, \tag{6}$$

where, k_f and k_b are the rates of formation and breakdown, respectively. It follows by the law of mass action [19] that

$$\frac{Dn}{D\hat{t}} = k_f m - k_b n = k_f (n_{max} - n) - k_b n, \tag{7}$$

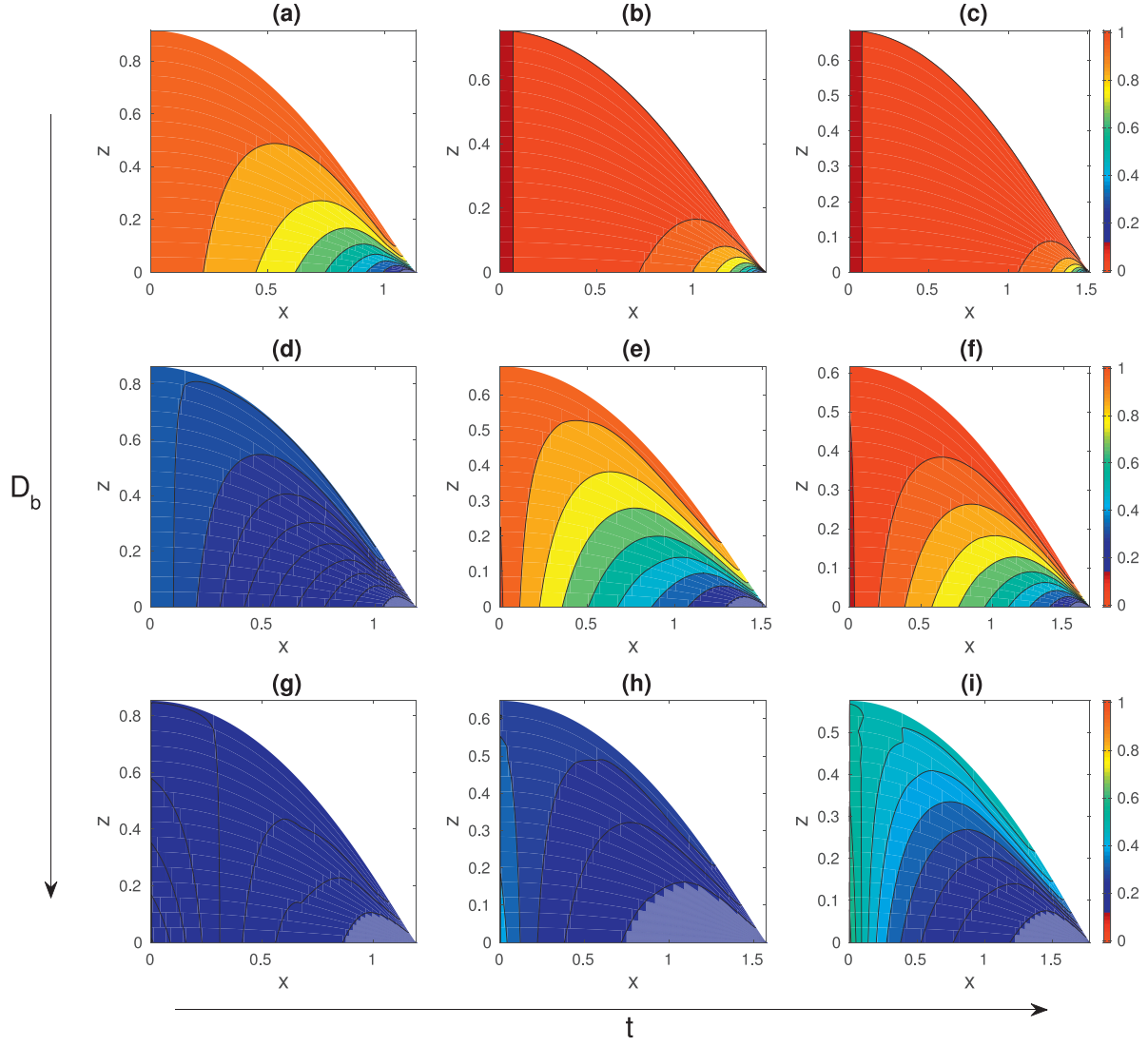

Fig. 6. Snapshots of the λ field at $t = 2$ (a, d, g), 20 (b, e, h) and 50 (c, f, i). We fix $B = 5$ and $\delta = 9$ and vary B, where $D_b = 1$ (a, b, c), $D_b = 10$ (d, e, f) and $D_b = 10$ (g, h, i). (For interpretation of the references to colour in this figure legend, the reader is referred to the web version of this article.)

where the formation and breakage rates are functions of the number of bonds and shear rate: $k_f = k_f(n, \dot{\hat{\gamma}})$ and $k_b = k_b(n, \dot{\hat{\gamma}})$. Note that these can be extended to be functions of a variety of physical parameters, thus providing a basis for the model to be generalised. We now introduce the structure parameter, λ, defining it as $\lambda = n/n_{max}$:

$$\frac{D\lambda}{Dt} = k_f(\lambda, \dot{\hat{\gamma}})(1-\lambda) - k_b(\lambda, \dot{\hat{\gamma}})\lambda. \tag{8}$$

Consistent with the commonly used Moore's model, as set out in [20], we take k_f to be constant and $k_b = k_b|\dot{\hat{\gamma}}|$ to get

$$\frac{D\lambda}{Dt} = k_f(1-\lambda) - k_b\lambda|\dot{\hat{\gamma}}|. \tag{9}$$

Thus, in Moore's model, 'structuration' is driven by Brownian motion, whereas 'destructuration' is precipitated by the shear rate. Additionally, we relate the structure to the viscosity, $\hat{\mu} = \hat{\mu}(\lambda)$. For simplicity, we take,

$$\hat{\mu} = \mu_0 + \lambda(\mu_\infty - \mu_0), \tag{10}$$

where μ_0 and μ_∞ correspond to the viscosity of the unstructured and structured states, respectively; in Section 4, we revisit the form of the viscosity dependence and investigate a more general model.

2.3. Scaling and cross-sectional averaging

We let L and H denote the characteristic length and height of the droplet, respectively, and apply the lubrication approximation, which assumes that the aspect ratio is small, $\epsilon = H/L \ll 1$. We then non-dimensionalise with the following scales:

$$(\hat{x}, \hat{z}) = L(x, \epsilon z), \quad (\hat{u}, \hat{w}) = U(u, \epsilon w), \tag{11}$$

$$\hat{p} = \frac{\sigma\epsilon}{L}p, \quad \hat{\mu} = \mu_0\mu, \quad \hat{t} = \frac{L}{U}t. \tag{12}$$

Assuming that the flow is driven by capillarity, we take the characteristic velocity to be, $U = \epsilon^3\sigma/\mu_0$. In addition, as in [14], we assume that $k_b \gg U/L$ or $k_f \gg U/L$, such that we can neglect convective effects in the structure evolution, Eq. (9), so that $D/Dt = \partial/\partial t$.

Substitution of the above scaling into the governing equations, and expanding in powers of ϵ, gives the following at leading-order

$$u_x + w_x = 0, \quad (\mu(\lambda)u_z)_z = p_x, \quad p_z = 0, \tag{13}$$

$$\lambda_t = \frac{1-\lambda}{D_b} - B\lambda|\dot{\gamma}|. \tag{14}$$

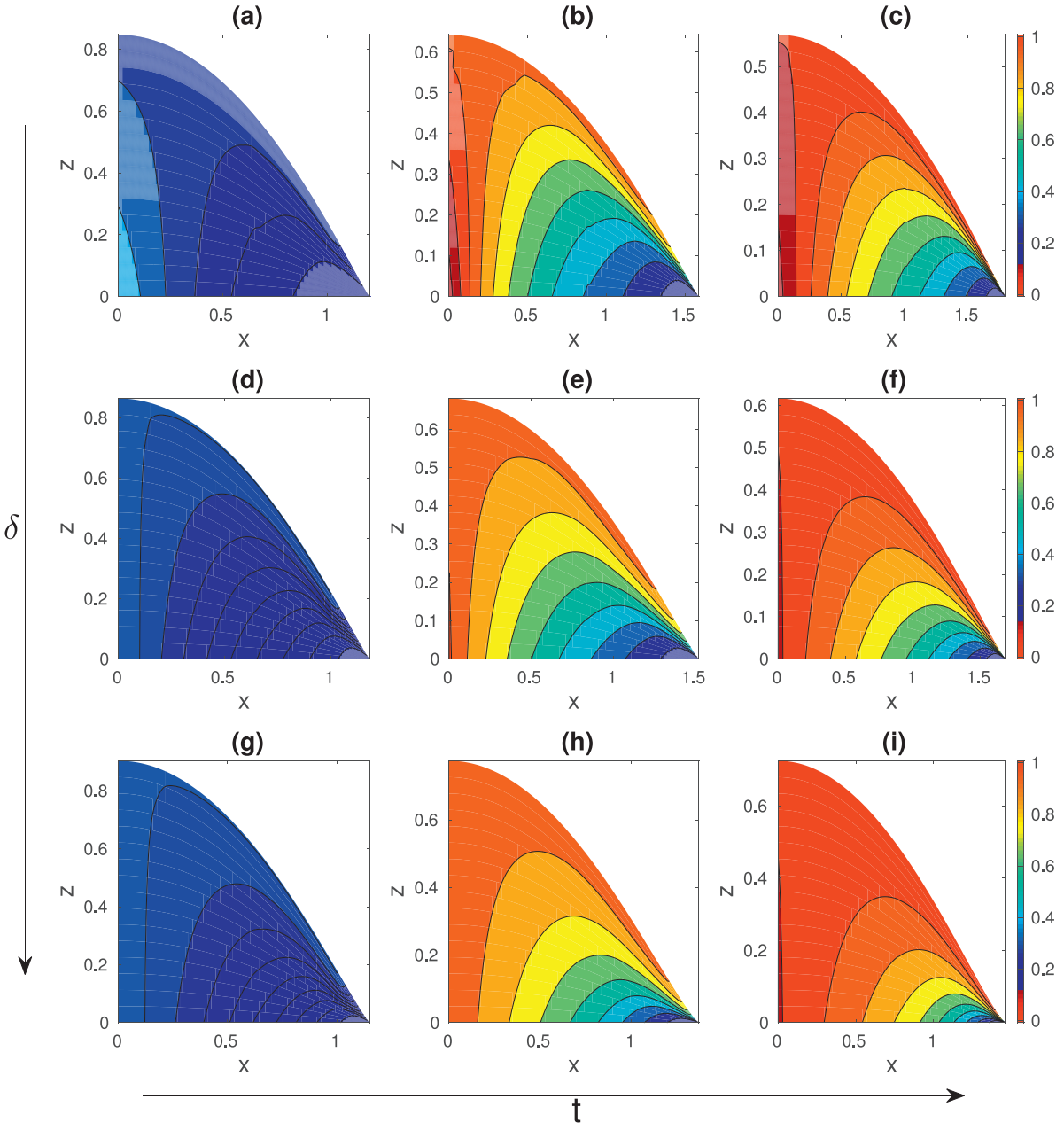

Fig. 7. Snapshots of the λ field at $t = 2$ (a, d, g), 20 (b, e, h) and 50 (c, f, i). We fix $D_b = 10$ and $B = 5$ and vary B, where $\delta = 1$ (a, b, c), $\delta = 9$ (d, e, f) and $\delta = 49$ (g, h, i). (For interpretation of the references to colour in this figure legend, the reader is referred to the web version of this article.)

The viscosity function now reads $\mu(\lambda) = 1 + \delta\lambda$, where $\delta = \mu_\infty/\mu_0 - 1$, and the leading-order strain rate is $\dot{\gamma} = u_z$. We have two additional dimensionless parameters: $D_b = U/(Lk_f)$; the ratio between the structuration and flow time-scales and $B = k_b/\epsilon$, denoting the relative strength of destructuration. The parameters D_b and B will be varied such that their respective effect upon the droplet can be investigated.

The interfacial stress boundary conditions now read

$$p = p_0 - h_{xx} \text{ and } u_z = 0 \text{ at } z = h, \tag{15}$$

where p_0 represents the non-dimensional atmospheric pressure and plays no further role in the analysis hereafter. Hence, we can set $p_0 = 0$ without loss of generality In addition, the kinematic condition is given by,

$$h_t + uh_x - w = 0 \text{ at } z = h, \tag{16}$$

alongside no-slip and no-penetration conditions at $z = 0$.

Now, Eq. (13) implies that the pressure is independent of the depth to leading order, thus the pressure is given by

$$p = -h_{xx}. \tag{17}$$

Thus, the second equation of Eq. (13) is solved alongside the tangential stress condition (15), to give,

$$\mu(\lambda)u_z = h_{xxx}(h - z). \tag{18}$$

Note that μ is a function of the microstructure and therefore of the depth, thus we can not easily integrate (18) as we would in the Newtonian case.

We now depth-average the continuity equation in Eq. (13) to generate an evolution equation for the interface following the imposition of the kinematic condition at $z = h$, (16):

$$h_t + (h\bar{u})_x = 0. \tag{19}$$

Here, we rewrite, $h\bar{u} = \int_0^h u \, dz = \int_0^h u_z(h - z) \, dz$, via integration by parts, where $\bar{u}$ is the depth-averaged horizontal component of the

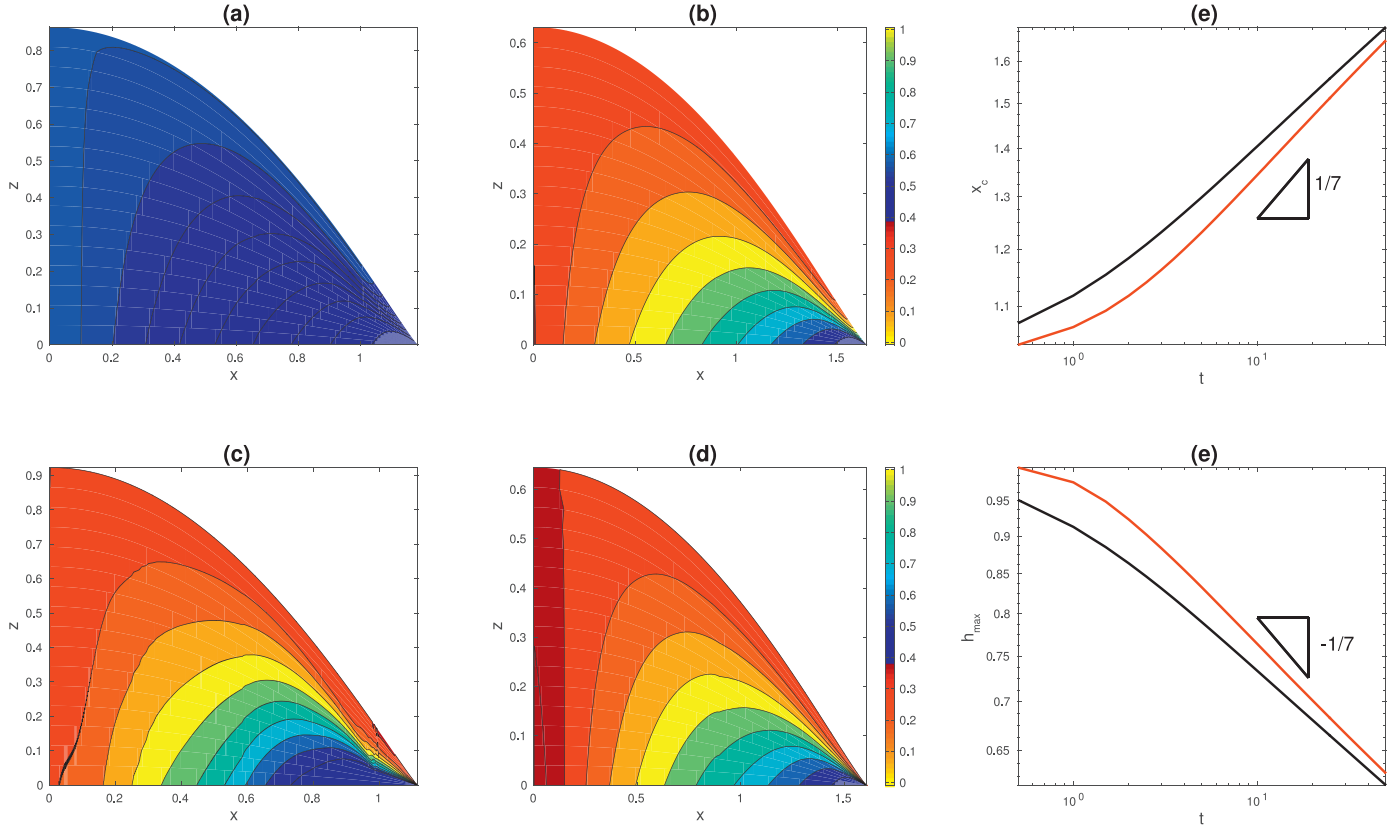

Fig. 8. Effect of initial level of drop structure on the spreading dynamics; λ fields for $\Lambda = 0$ and $\Lambda = 1$ are shown in (a) and (b) and (d) and (e) for $t = 2$, $t = 20$, respectively. Loglog plots for $x_c(t)$ and $h_{max}(t)$ are shown in (c) and (f), respectively, for $\Lambda = 0$ (black lines) and $\Lambda = 1$ (red lines). The rest of the parameters remain unchanged from those used to generate Fig. 2. (For interpretation of the references to colour in this figure legend, the reader is referred to the web version of this article.)

velocity. Substitution of Eq. (18) into Eqs. (14) and (19) yields

$$h_t + \left(h_{xxx} \int_0^h \frac{(h-z)^2}{1+\delta\lambda}\, \mathrm{d}z \right)_x = 0, \tag{20}$$

$$\lambda_t = \frac{1}{D_b}(1-\lambda) - B\lambda \frac{(h-z)}{1+\delta\lambda} |h_{xxx}|. \tag{21}$$

Henceforth, this will be referred to as the 1.5D model. Notably, Eq. (21) retains the z-dependence explicitly; it is natural to attempt to remove this explicit dependence using various closure approximations, as discussed below.

2.4. Simplifications

Here, we will explore two different types of simplifications. Firstly, we will use the methodology set out in [14], where an assumption is made regarding the depth profile of the fluidity. Secondly, we alternatively assume a depth profile for the structure parameter.

2.4.1. Fluidity closure

We next use the simplification presented in [14] in which the following depth profile of the fluidity is taken

$$\mu^{-1} = \mu_s^{-1} + \frac{z}{h}\left(\mu_f^{-1} - \mu_s^{-1}\right), \tag{22}$$

where μ_s and μ_f are the viscosities at the substrate and interface, respectively. These are related to the respective structure values by

$$\mu_i = 1 + \delta\lambda_i \quad i = s, f. \tag{23}$$

Chain rule is used, such that

$$\lambda_t|_{z=h\xi} = \lambda_t - \frac{\xi h_t}{h^2}\lambda_\xi, \quad \lambda_x|_{z=h\xi} = \lambda_x - \frac{\xi h_x}{h^2}\lambda_\xi, \tag{24}$$

Thereafter, we can substitute of $\xi = 0, 1$. Additionally, applying the no-slip and no-penetration at $\xi = 0$ and the kinematic condition at $\xi = 1$ allows us to obtain the following governing equations for $\lambda_s(x, t)$ and $\lambda_f(x, t)$,

$$\lambda_{st} = \frac{1}{D_b}(1-\lambda_s) - B\lambda_s h \frac{h_{xxx}}{1+\delta\lambda_s}. \tag{25}$$

$$\lambda_{ft} = \frac{1}{D_b}(1-\lambda_f), \tag{26}$$

Additionally, we have neglected convective effects for λ_f, which are shown to be negligible by either direct computation or by the method of characteristics. Computation of the integral in Eq. (20) gives,

$$h_t + \left[\frac{h^3 h_{xxx}}{12}\left(3\mu_s^{-1} + \mu_f^{-1}\right) \right]_x = 0. \tag{27}$$

2.4.2. Structure closures

Here, we assume that λ takes the form of a perturbation expansion

$$\lambda \sim \lambda_0(x,t) f(z) + \epsilon \lambda_1(x,z,t), \tag{28}$$

where we choose $f(z)$ such that $f'(h) = 0$ and enforce that $f(h) > f(0)$, inspection of Eq. (21), shows this to be true.

The lowest order polynomial which satisfies the above conditions is given by $f(z) = 1$. Thus, the structure across the depth is

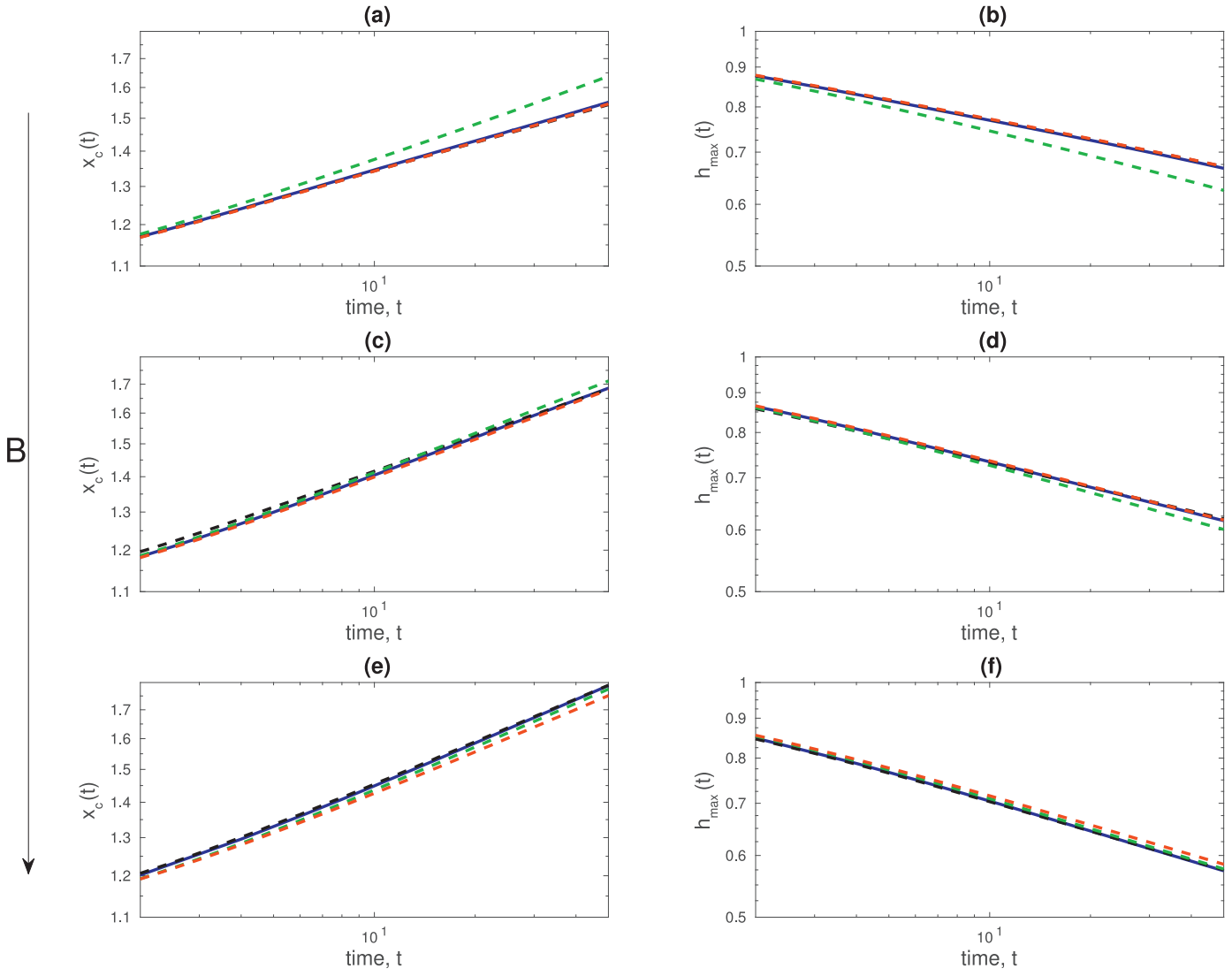

Fig. 9. Loglog plots of the leading edge position, $x_c(t)$ (a, c and e) and maximum height, h_{max} (b, d and f) showing comparisons between the predictions of the 1.5D and simplified models for $B = 0.5$, 5 and 50, depicted in (a)-(b), (c)-(d) and (e)-(f), respectively; $\Lambda = 0$, $D_b = 10$ and $\delta = 9$ remain fixed. The prediction of the 1.5D model are shown by black solid lines, while those of the fluidity, isostructural and cubic closure models are shown by the dashed red, black and green lines, respectively. (For interpretation of the references to colour in this figure legend, the reader is referred to the web version of this article.)

uniform in z and $\bar{\lambda} = \lambda_0(x,t)$, we refer to this as the 'isostructural' closure. We then compute the integral in Eq. (20) and depth-average Eq. (21) to obtain

$$h_t + \left[\frac{h^3 h_{xxx}}{3(1+\delta\bar{\lambda})}\right]_x = 0, \tag{29}$$

$$\bar{\lambda}_t = \frac{1}{D_b}(1-\bar{\lambda}) - \frac{B\bar{\lambda}}{2(1+\delta\bar{\lambda})} h|h_{xxx}|, \tag{30}$$

where $\bar{u}$ is expressed by

$$\bar{u} = \frac{h^2 h_{xxx}}{3(1+\delta\bar{\lambda})}. \tag{31}$$

In this system of equations the explicit depth dependence has been removed, and the partial differential equations only depend on x and t. However, the isostructural closure assumes that the depth variation of the microstructure has a small variance from average, which may not be sufficient for certain applications [15]. This is addressed via use of the following relation, which we refer to henceforth as the 'cubic' closure

$$f(z) = \frac{z}{h^2}(2\ h - z). \tag{32}$$

Following the same methodology as that employed above, Eqs. (20) and (21) become

$$h_t + [h_{xxx} I_h]_x = 0, \tag{33}$$

$$\lambda_{0t} + \frac{\lambda_0}{2h} h_t = \frac{1}{D_b}\left(\frac{3}{2} - \lambda_0\right) - \frac{3}{2} B h h_{xxx} I_\lambda, \tag{34}$$

where $I_h = \int_0^h \frac{(h-z)^2}{1+\delta f(z)\lambda_0}\,\mathrm{d}z$ and $I_\lambda = \int_0^h \frac{f(z)(h-z)}{1+\delta f(z)\lambda_0}\,\mathrm{d}z$, which are integrals that are evaluated using quadrature.

Note, inspection of Eqs. (28) and (32) indicate that $\lambda|_{z=0} = O(\epsilon)$, which is at odds with Eq. (21). Thus, we expect the predictions associated with the structure closures to diverge from those provided by Eq. (21) as $\lambda|_{z=0}$ grows to be larger than $o(\epsilon)$. We turn our attention to the discussion of the results which is presented next.

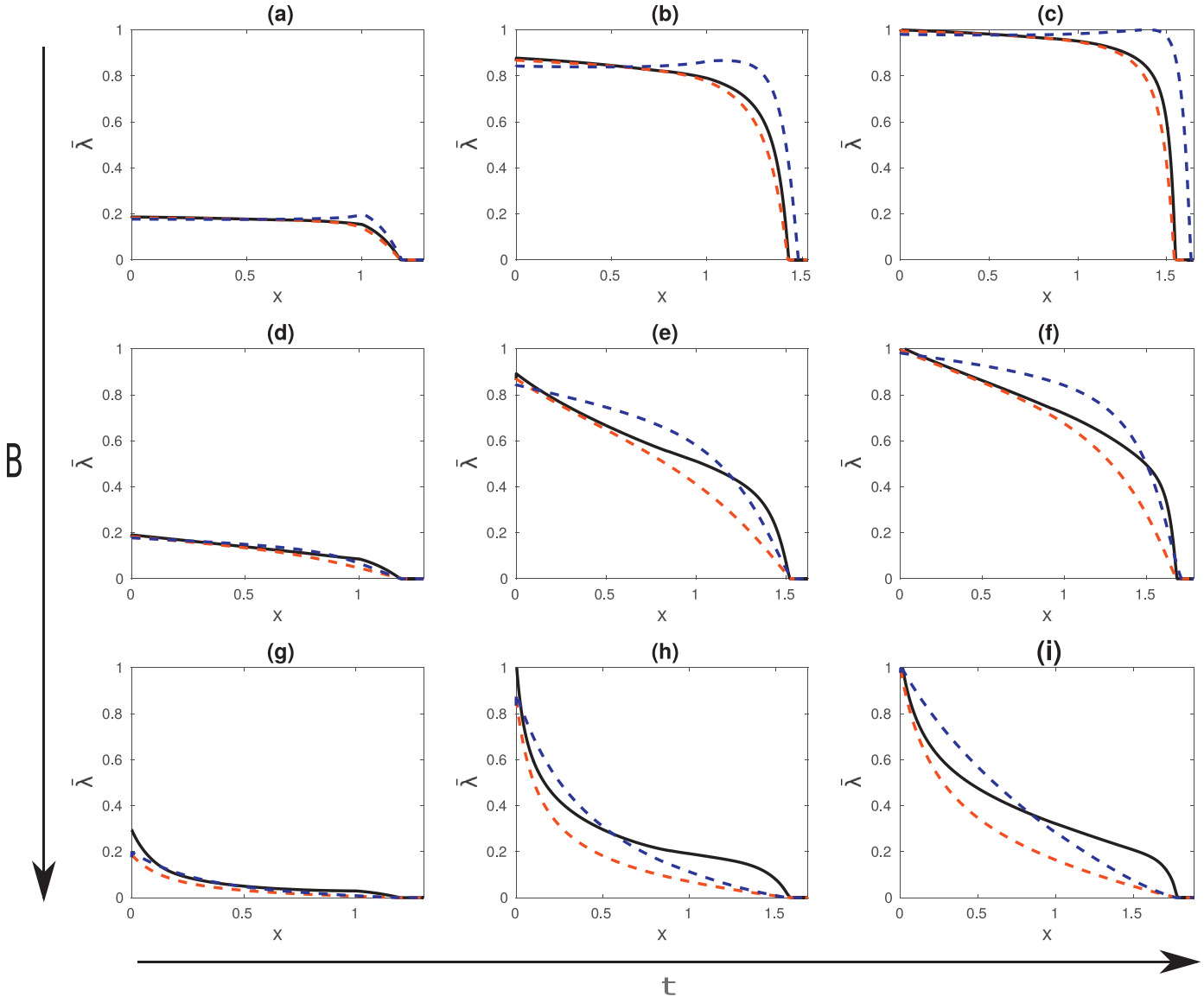

Fig. 10. Streamwise variation of the depth averaged λ, $\bar{\lambda}$ obtained from the 1.5D model (black line), and isostructural (red dashed line) and cubic (blue dashed line) closure models, for $B = 0.5$, 5 and 50 shown in (a)-(b), (c)-(d) and (e)-(f), respectively; the rest of the parameter values remain unaltered from Fig. 9. $\bar{\lambda}$ profiles are shown at $t = 2$ (a, d, g), 20 (b, e, h) and $t = 50$ (c, f, i). (For interpretation of the references to colour in this figure legend, the reader is referred to the web version of this article.)

3. Results

3.1. Numerical procedure

The evolution Eqs. (20) and (21) are solved using a numerical procedure, by first transforming the z co-ordinate as in Section 2.4, such that $\xi = z/h$. The numerical scheme employs finite-differences to discretise the spatial derivatives in both the x and ξ directions: centred differences are utilised over the whole of the computational domain except at the end points where one-sided differences are used. Typically, 1600 and 17 points are used in x and ξ (to evaluate the integrals in Eq. (20) using quadrature); convergence was achieved upon mesh-refinement. The solution is advanced in time using Gear's method, implemented with DASSL, [21].

Numerical solutions were obtained starting from the initial condition,

$$h(x,0) = \begin{cases} 1 - x^2 + h_\infty & |x| < 1, \\ h_\infty & |x| > 1, \end{cases} \tag{35}$$

$$\lambda(x,z,0) = \Lambda, \tag{36}$$

where Λ represents the initial degree of structuration in the droplet; Λ is taken to be zero for the majority of the simulations in this work. In Eq. (35), we have introduced a thin precursor film of height, h_∞, to remove singularities associated with moving contact lines. The initial condition described by Eqs. (35) and (36) corresponds, therefore to a droplet of constant curvature deposited on an ultra-thin precursor film with a prescribed constant level of microstructure. In addition, we switch off the term governing the increase in λ within the precursor film, so that it is only a device for dealing with the contact line singularity. We have checked that the precursor film has no effect on the computed solution when it is suitably small; we take $h_\infty = 10^{-4}$.

Numerical solutions are obtained subject to the following boundary conditions on h

$$h_x = h_{xxx} = 0 \quad \text{at } x = 0, \tag{37}$$

$$h_x = h_{xxx} = 0 \quad \text{at } x = \mathcal{L}, \tag{38}$$

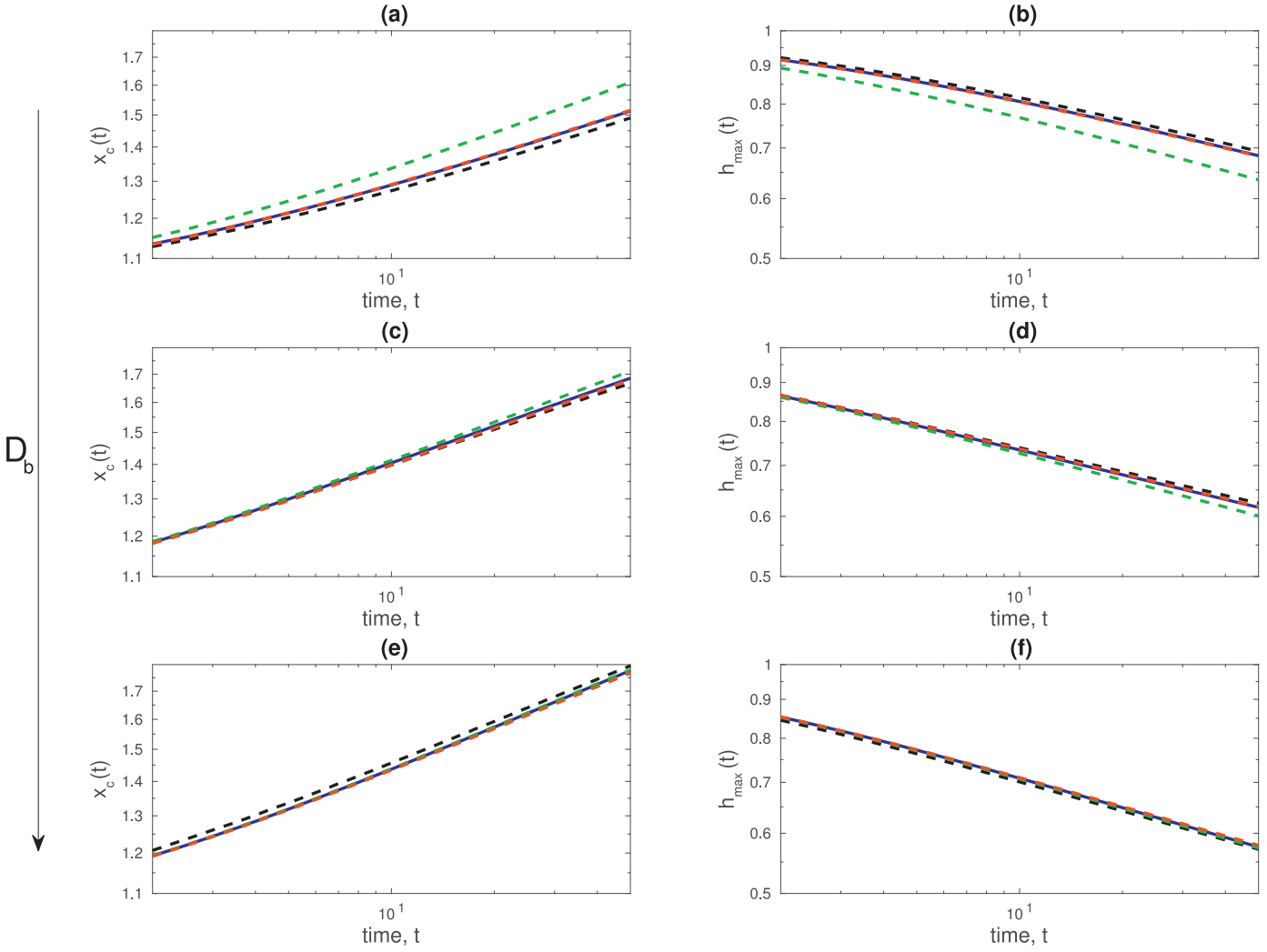

Fig. 11. Loglog plots of the leading edge position, $x_c(t)$ (a, c and e) and maximum height, h_{max} (b, d and f) showing comparisons between the predictions of the 1.5D and simplified models for $D_b = 1$, 10 and 100, depicted in (a)-(b), (c)-(d) and (e)-(f), respectively; $\Lambda = 0$, $B = 5$ and $\delta = 9$ remain fixed. The prediction of the 1.5D model are shown by black solid lines, while those of the fluidity, isostructural and cubic closure models are shown by the dashed red, black and green lines, respectively. (For interpretation of the references to colour in this figure legend, the reader is referred to the web version of this article.)

where $\mathcal{L}$ is the length of the computational domain. As additional checks, the mass of the fluid, $\int_0^\infty h\, dx$ is conserved during the computation. Finally, the code was validated against results presented in [14].

3.2. Parametric study

We begin by considering the evolution of a typical thixotropic droplet, as shown in Fig. 2. We set the parameters to be $B = 5$, $D_b = 10$ and $\delta = 9$, which reflect a balance between structuration and destructuration, we set $\Lambda = 0$ which reflects an initially unstructured drop. The thixotropic effects are characterised by the appearance of a structured region at the core of the droplet, and a highly-viscous skin near the interface. This to be expected upon inspection of Eq. (21), where we observe the shear rate, $\dot{\gamma}$, to be smallest near the centreline and interface of the droplet. Furthermore, the structured zones penetrate into the bulk of the droplet with increasing time. However, we do not expect the drop to become fully-structured due to the presence of large shearing near the contact line, creating a destructured region which facilitates drop spreading. This is shown more clearly in Fig. 2(d) which depicts an enlarged version of the contact line region and the associated λ field.

Fig. 3 displays the z-dependence of the structure parameter, λ, at $t = 20$ for $x = 0, 0.64, 1.28$ that coincide with the centreline, mid-stream and near-contact line locations (see Fig. 3(a)), for the same parameters as those used to generate Fig. 2. Inspection of the λ profiles depicted in Fig. 3(b)–(d) reveals that the z-dependence of λ is rather weak near the centreline, becoming progressively stronger as we move towards the contact line; moreover, λ attains its highest average value at $x = 0$, decreasing downstream. This trend can be explained by noting that structure-building and destructuration effects dominate the flow dynamics near the centreline and contact line regions, respectively. Furthermore, at every x location, the value of λ is highest at the interface $z = h$, and lowest at the wall, $z = 0$ since the shear stress is lowest and highest at the free surface and substrate, respectively; the difference between the maximal and minimal values of λ for a given x is largest in the contact line region.

Next, we present in Fig. 4 log-log plots of the temporal evolution of the contact line location, x_c, and the maximal film thickness, h_{max}, for different values of B, D_b, and δ. As is clearly seen in this figure, an enhanced spreading rate is promoted via an increase in B and D_b, and a decrease in the value of δ. We further quantify the effect of the 'thixotropic' parameters on the dynamics by examining the parametric dependence of the structure build-up

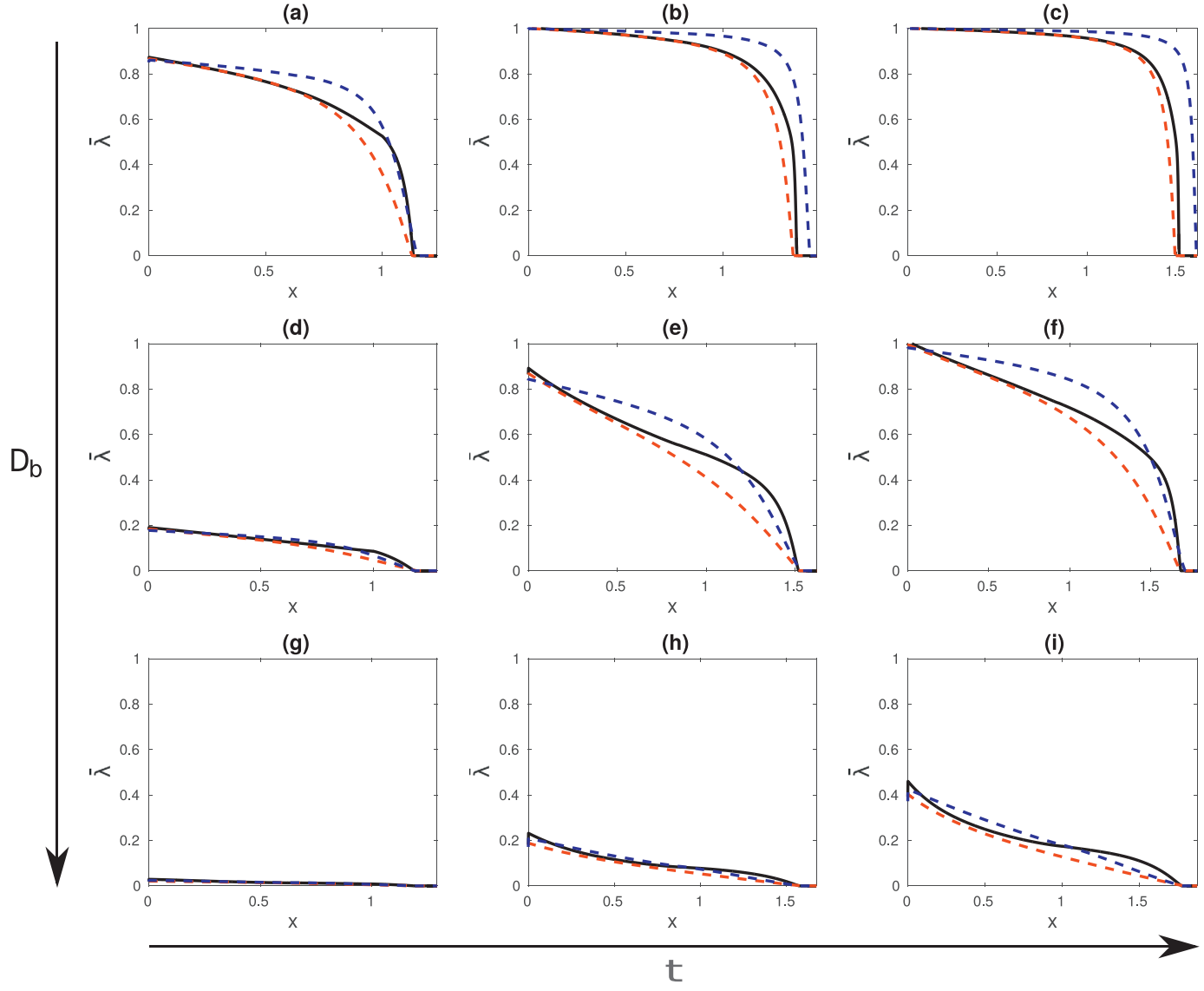

Fig. 12. Streamwise variation of the depth averaged λ, $\bar{\lambda}$ obtained from the 1.5D model (black line), and isostructural (red dashed line) and cubic (blue dashed line) closure models, for $D_b = 1$, 10 and 100 shown in (a)-(b), (c)-(d) and (e)-(f), respectively; the rest of the parameter values remain unaltered from Fig. 11. $\hat{\lambda}$ profiles are shown at $t = 2$ (a, d, g), 20 (b, e, h) and $t = 50$ (c, f, i). (For interpretation of the references to colour in this figure legend, the reader is referred to the web version of this article.)

spatio-temporal evolution on B, D_b, and δ. As shown in Figs. 5–7, increasing B and D_b, and decreasing the value of δ, have similar effects upon the droplet structure, which is commensurate with the trends shown in Fig. 4. With increasing B or D_b, the rate of structuration decreases and this has a marked effect on structure build-up in various parts of the drop. Specifically, for low values of B and D_b, it is seen in panels (a)–(c) of Figs. 5 and 6 that λ achieves its maximal value over the majority of the drop rapidly, except near the contact line. For the largest values of B and D_b studied, structuration is delayed considerably and appears to be confined to the centreline and near-interface regions. An increase in δ leads to an increase in the viscosity, which acts to retard the spreading such that there is more time for structuration; as can be seen in Fig. 7, however, the evolution of λ appears to be weakly-dependent on variations in δ.

We now examine the effect of the initial state of the drop on its evolution. In particular, the question is whether the influence of the drop initial internal structure, parametrised by Λ, will have a lasting effect on the spreading dynamics. In Fig. 8, we show the evolution of λ and the temporal variation of x_c starting from two initial conditions for λ: characterised by $\Lambda = 0$ and 1. Inspection of Fig. 8 shows clearly that the late-time dynamics exhibit a weak dependence on the initial conditions. Apart from a narrow strip near the centreline in which structuration is particularly intense, the λ field for the initially unstructured drop at $t = 20$ is very similar to that associated with $\Lambda = 1$ (see Fig. 8(b) and (d)). In Fig. 8(e), it is also seen that the contact line of the initially structured drop eventually catches up with that of the unstructured one.

3.3. Comparison of models

We now compare the predictions of the 1.5D model, Eqs. (20) and (21), with those provided by the evolution equations resulting from the simplifications set out in Section 2.4. To quantify the difference between the 1.5D and simplified models, we will consider the depth-averaged microstructure $\bar{\lambda} = \frac{1}{h}\int_0^h \lambda \, dz$, the maximum height, h_{max}, of the droplet and the position of the contact line, x_c. We begin by examining how variation in B affects the validity of the relevant closures. As shown in Fig. 9, the temporal variation of x_c and h_{max} exhibits a relatively weak dependence

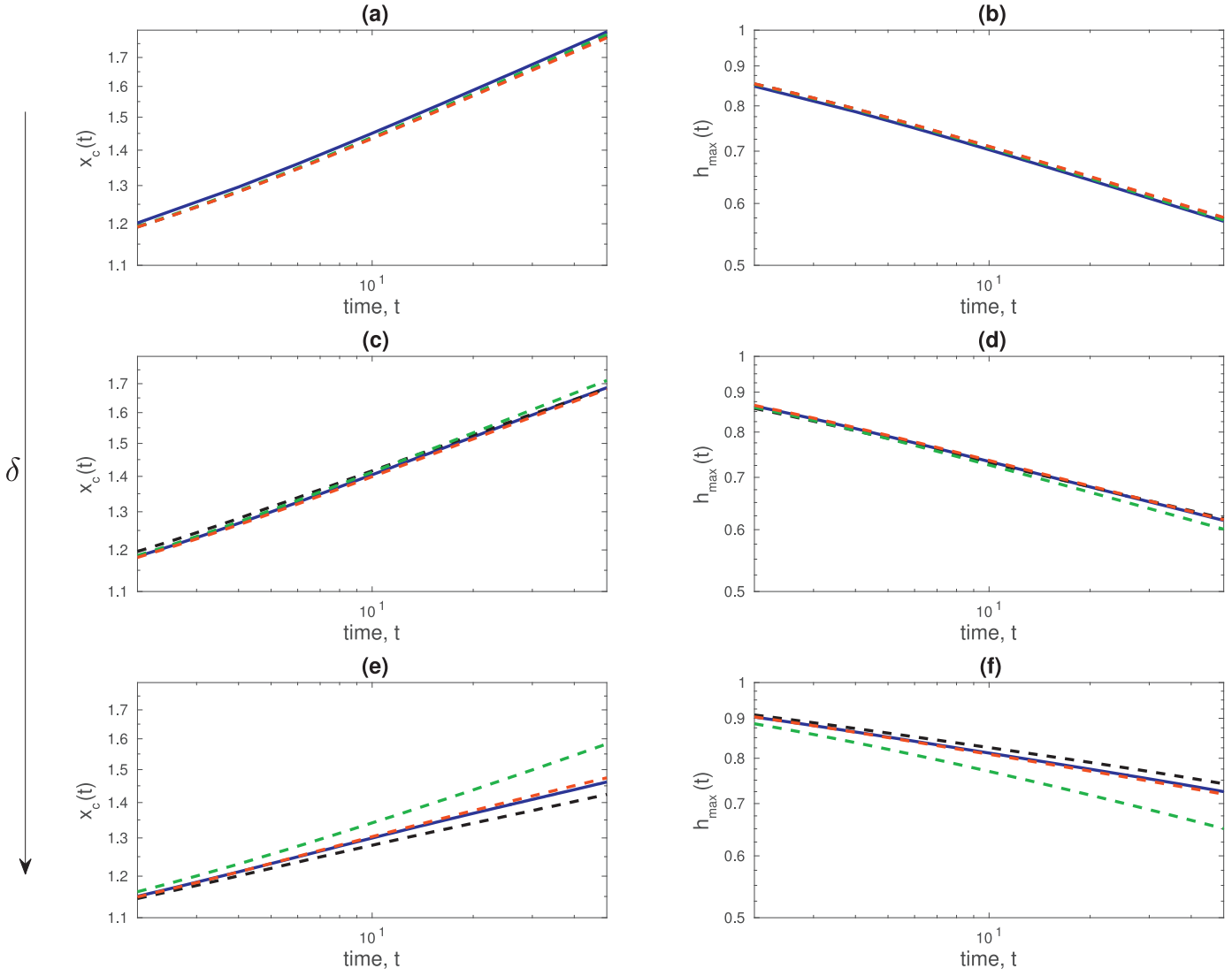

Fig. 13. Loglog plots of the leading edge position, $x_c(t)$ (a, c and e) and maximum height, h_{max} (b, d and f) showing comparisons between the predictions of the 1.5D and simplified models for $\delta = 1$, 9 and 49, depicted in (a)-(b), (c)-(d) and (e)-(f), respectively; $\Lambda = 0$, $B = 5$ and $D_b = 10$ remain fixed. The prediction of the 1.5D model are shown by black solid lines, while those of the fluidity, isostructural and cubic closure models are shown by the dashed red, black and green lines, respectively. (For interpretation of the references to colour in this figure legend, the reader is referred to the web version of this article.)

on the choice of closures, which are in good agreement with the predictions of the 1.5D model, with the possible exception of the cubic closure; this demonstrates the largest divergence from the predictions of the rest of the models for the smallest value of B studied. In Fig. 10, we show that for low B values, the isostructural model is in close agreement with the 1.5D model predictions in terms of the streamwise-variation of $\bar{\lambda}$ from early to late times, and out-performs the cubic closure model; this trend is reversed at large B. For intermediate B values, both of the closure models provide reasonably good approximations to the 1.5D model predictions. Similar trends in terms of agreement between the 1.5D and simplified models can be seen in Figs. 11 and 12.

We have also examined the effect of varying δ on the agreement between the simplified and 1.5D models for fixed B and D_b. As shown in Fig. 13, all closure models are in close agreement with the 1.5D model for all but the largest δ values examined at which considerable divergence can be seen; the largest such divergence is associated with the cubic closure model, while the fluidity closure model provides the closest agreement across the δ range explored. In terms of $\bar{\lambda}$, it is seen clearly from Fig. 14 that although the simplified models provide good qualitative agreement with the 1.5D model, the isostructural model is the most reliable one, exhibiting the closest such agreement over the range of δ studied.

Finally, we study briefly the case wherein the dependence of the viscosity on the structure parameter is altered such that it is given by the following expression

$$\mu = (1 - \lambda)^{-\delta}. \tag{39}$$

In Fig. 15, we show a comparison of the evolution of structure build-up within the drop associated with $\mu = 1 + \delta\lambda$ [see panels (a) and (b)], and with μ given by Eq. (39) (see panels (c) and (d), and (e) and (f), generated with $\delta = 1$ and 2, respectively). It is seen clearly that the degree of structuration increases markedly when the relation between μ and λ is modelled using Eq. (39); as shown in Fig. 15(f), for $\delta = 2$, λ achieves its maximal value over the large majority of the droplet, except for a narrow strip at the contact line.

It is also instructive to explore the effect of altering the $\mu(\lambda)$ model on the temporal evolution of the contact line location. As shown in Fig. 15(g), the switch to the model described by Eq. (39) leads to a decrease in the spreading rate. Intriguingly, the rate of structuration is sufficiently high for $\mu = (1 - \lambda)^{-2}$ that x_c

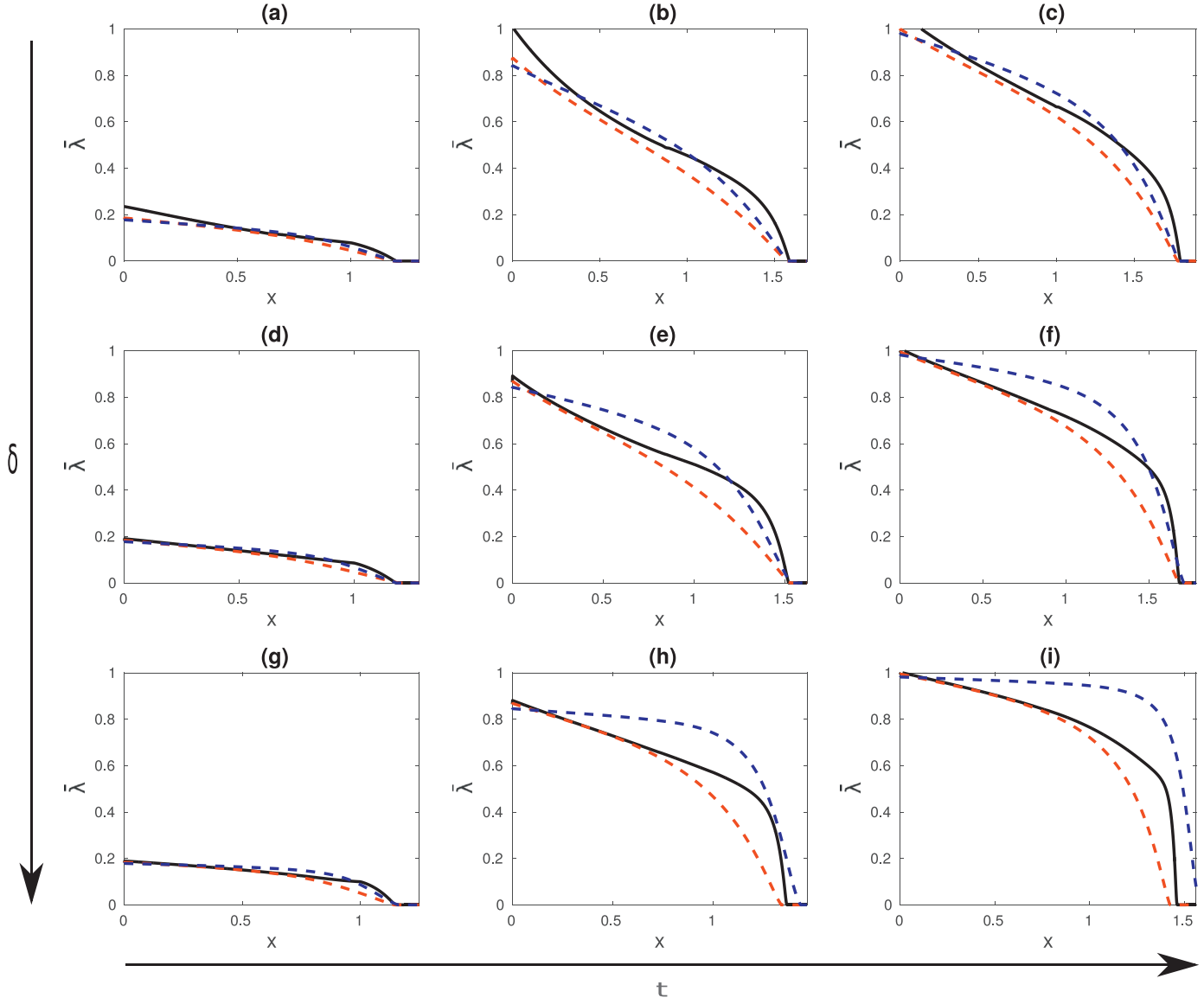

Fig. 14. Streamwise variation of the depth averaged λ, $\bar{\lambda}$ obtained from the 1.5D model (black line), and isostructural (red dashed line) and cubic (blue dashed line) closure models, for $\delta = 1$, 9 and 49 shown in (a)-(b), (c)-(d) and (e)-(f), respectively; the rest of the parameter values remain unaltered from Fig. 13. $\hat{\lambda}$ profiles are shown at $t = 2$ (a, d, g), 20 (b, e, h) and $t = 50$ (c, f, i). (For interpretation of the references to colour in this figure legend, the reader is referred to the web version of this article.)

reaches a constant value at long times, which signifies contact line pinning following a period of spreading. This behaviour has been observed previously in evaporating droplets containing particles, [22].

4. Concluding remarks

We have considered the two-dimensional spreading dynamics of a sessile drop in the presence of thixotropic effects. A hierarchy of models for the spreading were derived using the lubrication approximation for slender drops. The most complex model derived corresponds to a pair of coupled evolution equations for the interface and for a parameter that describes the level of structure build-up within the drop, and makes no assumptions regarding its dependence on the wall-normal direction; this was termed the "1.5D model" in this work. The remaining models introduce closure relations for this dependence, which result in the derivation of simplified, one-dimensional evolution equations. All of the models examined account for capillary-driven spreading, and thixotropy, which built in construction and shear-induced destructuration effects upon the structure and consequently on the viscosity. The models are solved numerically for a wide range of dimensionless parameters which reflect the relative significance of the various mechanisms in operation during the spreading process.

Our numerical results reveal that structuration is promoted in low-shear regions, which coincide with those near the centreline and the interface, and away from the moving contact line; the high level of shear in the latter region leads to destructuration as reflected by low values of the structure parameter. A comparison of the predictions of the 1.5D and simplified models is made, showing that the simplest closure model, which neglects the dependence of the structure parameter on the wall-normal direction, is the most robust; this model provides a very good approximation of the 1.5D model over the wide range of parameters explored. A discussion of the parameter space over which the simplified models breakdown was also provided. Finally, we show that for a particular choice of the dependence of the viscosity on the structure parameter, contact line pinning is observed.

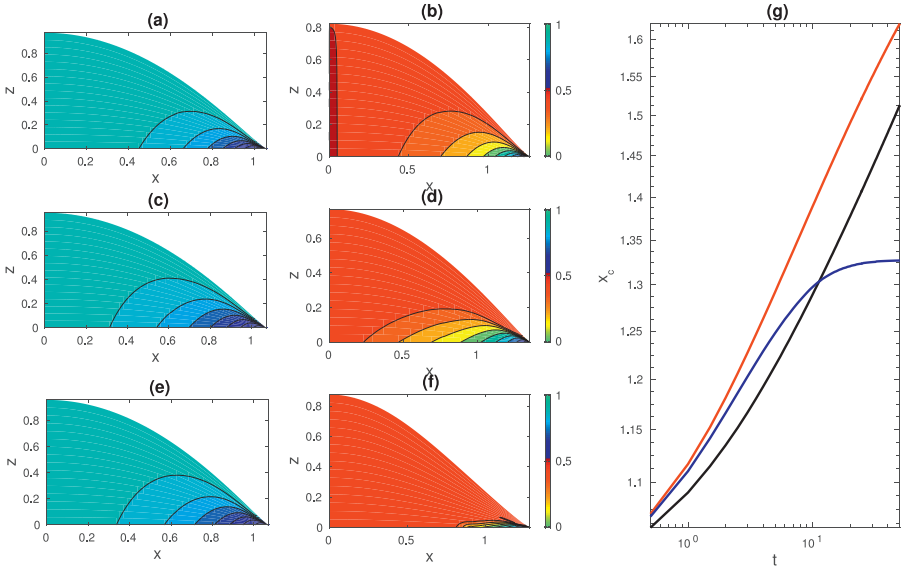

Fig. 15. Effect of altering the dependence of μ on λ on the evolution of the λ field, and contact line motion. Solutions for λ are shown in (a)-(b), (c)-(d), and (e)-(f), for $\mu = 1 + 9\lambda$, $\mu = (1-\lambda)^{-1}$, and $\mu = (1-\lambda)^{-2}$, respectively; the panels in the left and right columns correspond to solutions obtained at $t = 0.5$ and $t = 8$, respectively. The temporal evolution of x_c is shown in (g) in which the red, black, and blue curves are associated with the results shown in panels (a)-(b), (c)-(d), and (e)-(f), respectively. The rest of the parameters are $\Lambda = 0$, $B = 5$ and $D_b = 1$. (For interpretation of the references to colour in this figure legend, the reader is referred to the web version of this article.)

Acknowledgements

The authors acknowledge financial support from the Engineering and Physical Sciences Research Council, UK, through a PhD. studentship for A.S.U funded via the EPSRC Fluid Dynamics across Scales Centre for Doctoral Training.

References

[1] J. Mewis, N.J. Wagner, Thixotropy, Adv. Colloid Interface Sci. 147 (2009) 214–227.
[2] H.A. Barnes, Thixotropy - a review, J. Non-Newton Fluid Mech. 70 (1) (1997) 1–33.
[3] M. Renardy, Y. Renardy, Thixotropy in yield stress fluids as a limit of viscoelasticity, IMA J. Appl. Math. hxw031.
[4] M. Renardy, T. Wang, Development of shear bands for a model of a thixotropic yield stress fluid, J. Non-Newton Fluid Mech. 233 (2016) 5–12.
[5] K. Maki, Y. Renardy, The dynamics of a viscoelastic fluid which displays thixotropic yield stress behavior, J. Non-Newton Fluid Mech. 181 (2012) 30–50.
[6] B. Ebrahimi, S.-M. Taghavi, K. Sadeghy, Two-phase viscous fingering of immiscible thixotropic fluids: a numerical study, J. Non-Newton Fluid Mech. 218 (2015) 40–52.
[7] D. Pritchard, J.R.A. Pearson, Viscous fingering of a thixotropic fluid in a porous medium or a narrow fracture, J. Non-Newton Fluid Mech. 135 (2) (2006) 117–127.
[8] H. Huynh, N. Roussel, P. Coussot, Aging and free surface flow of a thixotropic fluid, Phys. Fluids (1994-present) 17 (3) (2005) 033101.
[9] D.R. Hewitt, N.J. Balmforth, Thixotropic gravity currents, J. Fluid Mech. 727 (2013) 56–82.
[10] H. Chanson, S. Jarny, P. Coussot, Dam break wave of thixotropic fluid, J. Hydraul. Eng. 132 (3) (2006) 280–293.
[11] R. Larson, Constitutive equations for thixotropic fluids, J. Rheol. (1978-present) 59 (3) (2015) 595–611.
[12] R.V. Craster, O.K. Matar, Dynamics and stability of thin liquid films, Rev Mod. Phys. 81 (3) (2009) 1131.
[13] A. Wachs, G. Vinay, I. Frigaard, A 1.5D numerical model for the start up of weakly compressible flow of a viscoplastic and thixotropic fluid in pipelines, J. Non-Newton Fluid Mech. 159 (1) (2009) 81–94.
[14] S. Livescu, R. Roy, L. Schwartz, Leveling of thixotropic liquids, J. Non-Newton Fluid Mech. 166 (7) (2011) 395–403.
[15] D. Sileri, K.C. Sahu, O.K. Matar, Two-fluid pressure-driven channel flow with wall deposition and ageing effects, J. Eng. Math. 71 (1) (2011) 109–130.
[16] D. Pritchard, S.K. Wilson, C.R. McArdle, Flow of a thixotropic or antithixotropic fluid in a slowly varying channel: the weakly advective regime, J. Non-Newton Fluid Mech. 238 (2016) 140–157.
[17] A. Mujumdar, A.N. Beris, A.B. Metzner, Transient phenomena in thixotropic systems, J. Non-Newton Fluid Mech. 102 (2) (2002) 157–178.
[18] M. Dembo, D. Torney, K. Saxman, D. Hammer, The reaction-limited kinetics of membrane-to-surface adhesion and detachment, in: Proceedings of the Royal Society of London B: Biological Sciences, 234,(1274), 1988, pp. 55–83.
[19] P. Érdi, J. Tóth, Mathematical Models of Chemical Reactions: Theory and Applications of Deterministic and Stochastic Models, Manchester University Press, 1989.
[20] J. Mewis, Thixotropy - a general review, J. Non-Newton Fluid Mech. 6 (1) (1979) 1–20.
[21] L.R. Petzold, A description of DASSL: a differential/algebraic system solver, in: Proceedings of IMACS World Congress, 1982, pp. 430–432.
[22] Á.G. Marín, H. Gelderblom, D. Lohse, J.H. Snoeijer, Order-to-disorder transition in ring-shaped colloidal stains, Phys. Rev. Lett. 107 (8) (2011) 085502.